GSA Data Repository 2018012

Hauri et al., 2018, CO2 content beneath northern Iceland and the variability of mantle carbon: Geology, https://doi.org/10.1130/G39413.1.

SUPPLEMENTARY INFORMATION

METHODS

Table DR1 contains the major, trace and volatile element compositions of 205 melt inclusions from NAL709, a quickly cooled tephra sample collected from the eruption vent of Borgarhraun, a monogenetic post-glacial eruption located in the Theistareykir segment of northern Iceland (Lat. 65.8234°, Long. -16.8665°). Major element compositions of melt inclusions and host olivines were determined by electron probe microanalysis (EPMA) at the Geophysical Laboratory, Carnegie Institution, using the following conditions: 15 kV accelerating voltage, 30 nA beam, spot mode (for the olivine) or beam defocused to 10 μm diameter (for the glasses). We processed the olivine analyses for matrix correction using the set of absorption coefficients from Pouchon and Pichoir (1991). Combined accuracy and precision is 2% for the major elements (all quoted uncertainties are 2-sigma); MnO was determined by laser ablation inductively coupled mass spectrometry (see below).

Volatiles (CO_2, H_2O, F, S, Cl) were determined by SIMS using methods described in Hauri et al. (2002, 2006) with the modification that ^{16}OH is collected for H_2O abundances rather than ^{1}H; total uncertainty (precision + accuracy) is ±7% for all volatiles. Selected trace elements (Li, Be, B, P, K, Sc, Ti, Cr, Sr, Y, Zr, Nb, Ba, La, Ce, Nd, Sm, Eu, Gd, Dy, Er, Yb, Hf) were determined by SIMS using a 10 nA beam of O^- (10–15 μm diameter) and detection of positive secondary ions with a nominal

acceleration voltage of + 10 kV. Energy filtering was employed (−135 ± 50 eV) as well as a moderate mass resolving power sufficient to resolve $^{27}Al^{3+}$ from ^{9}Be; calibration was performed in every session using the MPI-DING glasses KL2g, ML3Bg, GOR128g, GOR132g and BM90-21g; in addition we analyzed the in-house MORB glass standard ALV519-4-1 as a monitor of reproducibility. Trace element detection limits were measured using Herasil glass, and are very low (~50 ppb for Sr and Ba;~20 ppb for Hf and REE; ~5ppb for Nb). Combined accuracy and precision is 10% for all the trace elements reported.

Selected trace elements that can be difficult to measure accurately by SIMS (V, Mn, Co, Ni, Cu, Zn, Rb, Cs, Pb, Th, U), as well as several elements overlapping with SIMS (Nb, Ba, Hf) were determined by laser-ablation inductively coupled plasma mass spectrometry (LA-ICPMS) using a Photon Machines 193nm excimer laser and a Thermo iCapQ ICP-MS. A 35 μm diameter beam was used to ablate material into a pure He gas stream (0.6 liters/min) injected into a pure Ar gas stream (1.4 liters/min) at a rate of 40 Hz for a total of 400 shots (ablation rate 0.1 μm/shot). Calibration was performed in every session using the MPI-DING glasses (KL2g, ML3Bg, GOR128g, GOR132g and BM90-21g) and USGS glasses (BCR-2g, BHVO-2g, BIR-1g); in addition we analyzed the in-house MORB glass standard VE-32 as a monitor of reproducibility. Detection limits were in the single parts-per-billion range except for Sc which has an isobaric interference from SiO; ablation of pure forsterite (0.07 ppm Sc) was used to correct the SiO interference on Sc. Combined accuracy and precision is 6% or better for these trace elements; SIMS and LA-ICPMS data agree to within 8% for Nb, 10% for Ba and 15% for Hf.

For melt inclusions that contained a vapor bubble, bubble diameters were either measured by SEM when exposed at the surface, or by optical microscopy (±10-20%) using a calibrated scale; melt inclusion axes were measured with an SEM with an uncertainty of ±3%. We estimated the amount of vapor and the moles of H_2O and CO_2 in the shrinkage bubbles using the ideal gas law (IGL, $n=PV/RT$) where n is the total moles of gas in the shrinkage bubble. For the IGL calculation, our pressure estimate (P) and molar proportions of H_2O and CO_2 come from the vapor saturation pressure determined from the H_2O and CO_2 contents measured on the melt inclusion glass applied to the vapor saturation model of Dixon et al. (1995). We used a closure temperature of 900°C for H_2O-CO_2 exchange in these rapidly-cooled inclusions, and the melt inclusion volume was calculated from the equation for the volume of an ellipsoid, using the measured long and short axes of the melt inclusion and assuming the two short axes of the ellipsoid are equal. From these constraints, we calculated the masses of H_2O and CO_2 in each shrinkage bubble, and added these masses back into the composition of the melt inclusion, thereby calculating a bulk inclusion H_2O and CO_2 content for each melt inclusion that contained a shrinkage bubble. In these calculations, the amount of H_2O in the shrinkage bubble was vanishingly small, and CO_2 contained in the shrinkage bubble never exceeded 50% of the bulk CO_2 content.

Table DR2 contains major, volatile and trace element abundances (and radiogenic isotope data where it exists) for mid-ocean ridge basalts containing CO_2 and Nb data on the same sample, as recorded in the PetDB petrological database (161 samples). These samples were chosen by ranking the samples by CO_2/Nb data and selecting the samples in the upper 90th percentile, excluding samples from transform fault systems (the

Siqueiros data of Saal et al. (2002) and QDG data of Shimizu et al. (2016) are considered separately). The data set was filtered to include only samples with CO_2 determined by either SIMS or FTIR, and contains all of the vapor-undersaturated MORB samples (5 samples) described in Michael and Graham (2015) which are not from transform fault regions or from the study of Shimizu et al. (2016). In this group of 15 samples, we did not use the pressure of vapor saturation to evaluate whether or not they were undersaturated in CO_2. Instead we relied on their correlated abundances of CO_2 and Nb-Rb-Ba as an indication that the samples did not degas CO_2. There exist several models based on experimental data that calibrate vapor saturation pressure with CO_2+H_2O contents in mafic melts (Holloway & Blank, 1994; Dixon & Stolper, 1995; Papale, 1999; Newman & Lowenstern, 2002; Papale et al., 2006; Iacono-Marziano et al., 2012; Ghiorso & Gualda, 2015), and they all give somewhat different vapor saturation pressures, thus we have not relied on estimated vapor saturation pressures to determine whether samples have lost CO_2 by degassing.

To determine the CO_2/Nb ratio of the melt inclusion population, we calculated the CO_2/Nb ratio of each melt inclusion and then calculated the simple arithmetic mean of the population. The same method was used to calculate the CO_2/Nb ratio of melt inclusion populations from the Siqueiros Fracture Zone (Saal et al., 2002) and the equatorial mid-Atlantic Ridge (Le Voyer et al. 2016), and the vapor-undersaturated MORB sample suites described by Cartigny et al. (2008) and Shimizu et al. (2016), and the top 10% MORB samples described above. Uncertainties on the CO_2/ITE ratios of the data populations were calculated as 2 standard errors of the population.

COMPARISON WITH PUBLISHED DATA

Studies reporting CO_2 abundances in submarine glasses and melt inclusions normally display large scatter due to heterogeneous distributions of CO_2-rich bubbles (vesicles) within submarine samples, and the presence of shrinkage bubbles in melt inclusions whose presence is not typically accounted for (Moore et al., 2015). As a result, for the global MORB database as a whole, neither submarine MORB glasses nor most MORB melt inclusions display correlations of CO_2 with non-volatile trace elements (Fig. 4), although certain samples plot at CO_2/ITE ratios similar to the Borgarhraun melt inclusions.

Several prior studies have focused attention on the highest CO_2/Nb ratios among a group of melt inclusions, arguing that melt inclusions with the highest CO_2/Nb most closely approach the composition of the undegassed magma, and that lower CO_2/Nb ratios are produced by degassing of CO_2 during magma ascent from depth (Wanless and Shaw, 2012; Wanless et al., 2014; Rosenthal et al., 2015). This approach is problematic; the highest CO_2/Nb ratio among the Borgarhraun melt inclusions (961) occurs in a spinel-hosted inclusion corrected for the presence of a shrinkage bubble, and is more than twice the average CO_2/Nb of the population. The highest bubble-free melt inclusion from Borgarhraun has a CO_2/Nb of 598, which is still 50% higher than the population average. Further insight into the origin of the data scatter is obtained from the systematics of the non-volatile trace elements; (Slater et al., 2001; Maclennan et al., 2003) demonstrated that the rare-earth element (REE) patterns of many populations of Iceland melt inclusions could be accurately fit by invoking incomplete mixing of polybaric near-fractional melts derived from adiabatic upwelling of a column of mantle. In Figure 3 we have tested this model for the CO_2-Nb variation, using appropriate C and Nb partition coefficients

between mantle minerals and silicate melts (Rosenthal et al., 2015). We used pHMELTS (Asimow et al., 2001) (Smith and Asimow, 2005) to model the 1D adiabatic melting process, with a mantle potential temperature of 1410°C (corresponding to 1450°C at 3 GPa), and a residual melt porosity of 1.5% which serves as a threshold above which melt ascent and mixing becomes possible. In this model melting begins at 3.0 GPa and ceases at 0.85 GPa, a pressure that corresponds approximately to the base of the crust beneath northern Iceland, yielding an overall degree of melting of 17%. For a mantle source with 75.4 ppm CO_2 and 0.193 ppm Nb, this melting model produces a curved trajectory of incremental melt compositions that skirts the lower bound of the CO_2-Nb data, while families of linear mixing trajectories among the incremental melt compositions explains well the scatter of the Borgarhraun CO_2-Nb data (Fig. 3).

We illustrate this point to emphasize that erroneous estimates of the CO_2/Nb of mantle sources can arise when focusing on the highest CO_2/Nb ratio among a population of melt inclusions. While such variations can be due to degassing (Wanless and Shaw, 2012; Wanless et al., 2014), they can also result as a normal part of the range in CO_2/Nb ratios of incremental melts produced during near-fractional melting due to the slight difference melt-solid partition coefficients of CO_2 and Nb, and it is these near-fractional incremental melt compositions (and their mixtures) that are often preserved in melt inclusions hosted by primitive high-Mg# phenocrysts. The best approach to estimating the CO_2/Nb ratio of the mantle source is to first account for CO_2 partitioning into melt inclusion shrinkage bubbles, then to look for a correlation of CO_2 with Nb or other non-volatile trace elements. Well-correlated CO_2 and Nb indicate the absence of degassing and thus a record of the mantle source ratio, but if no correlation is found then it can be

reasonably assumed that the melt had lost CO_2 via degassing prior to inclusion entrapment. As a result, for a population of degassed melt inclusions it is not possible to recover the pre-degassing CO_2/Nb ratio with any degree of precision.

AVERAGE AND LOCAL MANTLE CO_2 ABUNDANCES

Stracke et al. (2003) observed that whole rock samples from the Borgarhraun flow were isotopically heterogeneous, and Maclennan et al. (2003) used major and trace element compositions of melt inclusions from Borgarhraun to demonstrate that the array of melt compositions present in the Borgarhaun mantle came from the same distribution of melt compositions that represent the Theistareykir segment as a whole. McKenzie et al. (2004) demonstrated that isotopic variations correlate with the concentrations of incompatible trace elements both in the Borgarhraun flow and in the Theistareykir segment, while Maclennan (2008) showed that correlated variations in Pb isotopes and trace elements in melt inclusions from the Reykjanes Peninsula demonstrate a dominant role for mixing of melts from heterogeneous sources in generating the chemical and isotopic variability of Icelandic basalts. Thus some of the small variability in CO_2/Nb ratios may represent melt mixing superimposed upon populations of near-fractional melts from a heterogeneous mantle, and if so then it is probable that the CO_2/Nb ratio of the Borgarhraun melt inclusion population is dominated by melts from the more enriched mantle components beneath the Theistareykir segment.

We use all four non-volatile trace elements (Th, Nb, Rb, Ba) to provide multiple estimates of mantle source CO_2 content. The CO_2 and ITE contents observed in the Borgarhraun melt inclusions span half of the range displayed by MORB, between the depleted Siqueiros magmas (CO_2/Nb = 230) and the enriched magmas of the 14°N MAR

region (CO_2/Nb = 534). Given that the six sample suites examined here span the entire range of trace element depletion and enrichment observed in MORB, we conclude that upper-mantle CO_2/Nb ratios at other MOR segments are unlikely to vary significantly outside this range (factor of 2.4). Assuming a global average CO_2/Nb ratio of 435 (Table 1, ALL-MORB), with a melt production rate of 21±3 km^3/yr (Crisp, 1984), crustal density of 2700 kg/m^3, and an average MORB Nb content of 3.62±0.36 ppm (Gale et al., 2013), the global average Nb flux across the crust-mantle boundary at mid-ocean ridges amounts to $2.23\pm0.36\times10^9$ mol/yr, and this translates into an average global CO_2 flux of $2.03\pm0.36\times10^{12}$ mol/yr for the present-day mid-ocean ridge system. This flux is within 20% of that calculated by Michael and Graham (2015). The average CO_2 flux estimated from Nb, Th, Rb and Ba fluxes at mid-ocean ridges is $2.38\pm0.46\times10^{12}$ mol/yr (Table 1). The average MOR CO_2 flux thus calculated is at the low end of the range of most published estimates, but within the ranges estimated by Cartigny et al. (2008) and Burton et al. (2013). With an average $CO_2/^3He$ molar ratio of $2.5\pm1.0\times10^9$ (Marty and Tolstikhin, 1998), this constrains the average MORB ^3He flux to be 953±325 mol/yr.

This global average of course does not apply directly to specific geographic areas such as Borgarhraun and the other locales in Table 1, as trace element compositions and radiogenic isotope ratios are known to vary significantly along the global mid-ocean ridge system (Jenner and O'Neill, 2012; Gale et al., 2013; Kelley et al., 2013); thus changes in source composition and magma production rate will cause CO_2 output from ridges to vary one locale to the next. In order to estimate local CO_2 fluxes, we must have knowledge of the mantle Th-Nb-Rb-Ba abundances at each location. To estimate mantle ITE compositions we approximate the compositional and isotopic range in MORB as a

mixture between two depleted MORB mantle sources, one representing the depleted extreme of the MORB range (D-DMM) and the other at the enriched extreme (E-DMM) as described by Shimizu et al. (2016) but with the small adjustments made to the D-DMM component in the CO_2 (150 ppm), Rb (0.36 ppm), Ba (3.90) and Th (0.047) concentrations, in order to provide a best fit to the six MORB population averages (Fig. 6). In this model, we use the Nd isotope composition of the sample to determine the extent of mixing between D-DMM and E-DMM, and from this mixture the trace element composition can be derived given appropriate D-DMM and E-DMM endmember compositions. For D-DMM we use the trace element estimate of Workman and Hart (2005) with epsilon-Nd = +10.5 and CO2 = 150 ppm, but with small adjustments made in Rb (0.36 ppm), Ba (3.90) and Th (0.047) concentrations in order to provide a best fit to the six MORB population averages (Fig. 6). The Nd isotope composition of each sample or sample population thus determines the non-volatile ITE concentrations that are used to provide estimates for mantle source CO_2 based on CO_2/ITE ratios. These estimates are compiled in Table 1, and demonstrate that mantle CO_2 abundances can vary by more than a factor of ten at the local scale. Although this model fails to predict the CO_2/ITE ratios of the equatorial MAR melt inclusions of Le Voyer et al. (2016), we note that this MAR sample has the highest $^{143}Nd/^{144}Nd$ known among all MORB and thus may have originated from an endmember more depleted, or with older time-integrated Sm/Nd, than the endmember Nd isotope composition chosen by Shimizu et al. (2016).

Supplemental References

Asimow, P.D., Hirschmann, M.M., and Stolper, E.M., 2001, Calculation of peridotite partial melting from thermodynamic models of minerals and melts, IV. Adiabatic decompression and the composition and mean properties of mid-ocean ridge basalts: Journal of Petrology, v. 42, p. 963–998, https://doi.org/10.1093/petrology/42.5.963.

Crisp, J.A., 1984, Rates of magma emplacement and volcanic output: Journal of Volcanology and Geothermal Research, v. 20, p. 177–211, https://doi.org/10.1016/0377-0273(84)90039-8.

Hauri, E., Wang, J., Dixon, J.E., King, P.L., and Mandeville, C., 2002, SIMS analysis of volatiles in silicate glasses 1. Calibration, matrix effects and comparisons with FTIR: Chemical Geology, v. 183, p. 99–114, https://doi.org/10.1016/S0009-2541(01)00375-8.

Hauri, E.H., Shaw, A.M., Wang, J., Dixon, J.E., King, P.L., and Mandeville, C.W., 2006, Matrix effects in hydrogen isotope analysis of silicate glasses by SIMS: Chemical Geology, v. 235, p. 352–365, https://doi.org/10.1016/j.chemgeo.2006.08.010.

Maclennan, J., 2008, Concurrent mixing and cooling of melts under Iceland: Journal of Petrology, v. 49, p. 1931–1953, https://doi.org/10.1093/petrology/egn052.

Maclennan, J., McKenzie, D., Gronvold, K., Shimizu, N., Eiler, J.M., and Kitchen, N., 2003, Melt mixing and crystallization under Theistareykir, northeast Iceland: Geochemistry Geophysics Geosystems, v. 4, p. n/a–n/a, https://doi.org/10.1029/2003GC000558.

Marty, B., and Tolstikhin, I.N., 1998, CO_2 fluxes from mid-ocean ridges, arcs and plumes: Chemical Geology, v. 145, p. 233–248, https://doi.org/10.1016/S0009-2541(97)00145-9.

McKenzie, D., Stracke, A., Blichert-Toft, J., Albarede, F., Gronvold, K., and O'Nions, R.K., 2004, Source enrichment processes responsible for isotopic anomalies in oceanic island basalts: Geochimica et Cosmochimica Acta, v. 68, p. 2699–2724, https://doi.org/10.1016/j.gca.2003.10.029.

Pouchou, J.-L., and Pichoir, F., 1991, Quantitative analyses of homogenous or stratified microvolumes applying the model "PAP," *in* Heinrich, K. F., and Newbury, D. E., eds., Electron Probe Quantification: New York, Plenum Press, p. 31–75, https://doi.org/10.1007/978-1-4899-2617-3_4.

Rosenthal, A., Hauri, E.H., and Hirschmann, M.M., 2015, Experimental determination of C, F and H partitioning between mantle minerals and carbonated basalt; CO_2/Ba and CO_2/Nb systematics of partial melting, and the CO_2 contents of basaltic source regions: Earth and Planetary Science Letters, v. 412, p. 77–87, https://doi.org/10.1016/j.epsl.2014.11.044, erratum can be found at http://dx.doi.org/10.1016/j.epsl.2015.03.030.

Slater, L., McKenzie, D., Gronvold, K., and Shimizu, N., 2001, Melt generation and movement beneath Theistareykir, NE Iceland: Journal of Petrology, v. 42, p. 321–354, https://doi.org/10.1093/petrology/42.2.321.

Smith, P.M., and Asimow, P.D., 2005, Adiabat_1ph: A new public front-end to the MELTS, pMELTS, and pHMELTS models: Geochemistry Geophysics Geosystems, v. 6, p. Q02004, https://doi.org/10.1029/2004GC000816.

Wanless, V.D., and Shaw, A.M., 2012, Lower crustal crystallization and melt evolution at mid-ocean ridges: Nature Geoscience, v. 5, p. 651–655, https://doi.org/10.1038/ngeo1552.

Wanless, V.D., Behn, M.D., Shaw, A.M., and Plank, T., 2014, Variations in melting dynamics and mantle compositions along the Eastern Volcanic Zone of the Gakkel Ridge: Insights from olivine-hosted melt inclusions: Contributions to Mineralogy and Petrology, v. 167, p. 1005–1027, https://doi.org/10.1007/s00410-014-1005-7.

Supplementary Tables

Please see separate Excel spreadsheet (2018012_Tables.xlsx) containing the following:

Table DR1: Iceland Melt Inclusions

Table DR2. Published MORB data for samples in the upper 10% of CO2/Nb ratios (ranked)

Supplemental Figures

Figure DR1. (A) Transmitted light, and (B) reflected light photos of olivine-hosted melt inclusions from Borgarhraun. The olivine crystal is 3mm across the long axis; circular black depressions are 35 μm diameter laser ablation craters.

Figure DR2. CO_2 versus Nb for Borgarhraun melt inclusions (red filled circles) compared with near-fractional melts of a mantle composition with 75 ppm CO_2 and 0.193 ppm Nb (red curve, see text). Blue line is a regression line through the melt inclusion data, black line is a mixing line between the most enriched and most depleted of the incremental melts. The data are bound by the compositions of incremental melts along the red curve, and families of mixing lines connecting enriched and depleted incremental melts. Inset shows the full range of incremental melt compositions.

Figure DR3. These high-precision MORB CO2 data sets shown with the global published data on olivine-hosted melt inclusions (panel B, PetDB and Georoc databases).

Figure DR4. (A) Average CO_2/Rb and CO_2/Ba ratios for the six mid-ocean ridge regions that exhibit CO2-ITE correlations; Atlantic locales are shown in green, Pacific locales are shown in blue. CO_2/Rb and CO_2/Ba ratios are nearly homogeneous and show no distinctions between ocean basins. (B) Average CO_2/Nb and CO_2/Th ratios are heterogeneous and correlated, with Atlantic locales being 70-100% higher than Pacific locales.

Figure DR5. La/Sm and CO_2/Nb ratios of individual samples and melt inclusions from the sample groups discussed in this study, group by Atlantic (14°N MAR, equatorial MAR, Iceland) and Pacific (Siqueiros, QGD, Top 10% MORB). Average CO_2/Nb and La/Sm are higher in the Atlantic vs Pacific groups, but overall there is no correlation, and the full range of CO_2/Nb ratio is expressed at intermediate La/Sm that is exhibited by both groups.

Figure DR1

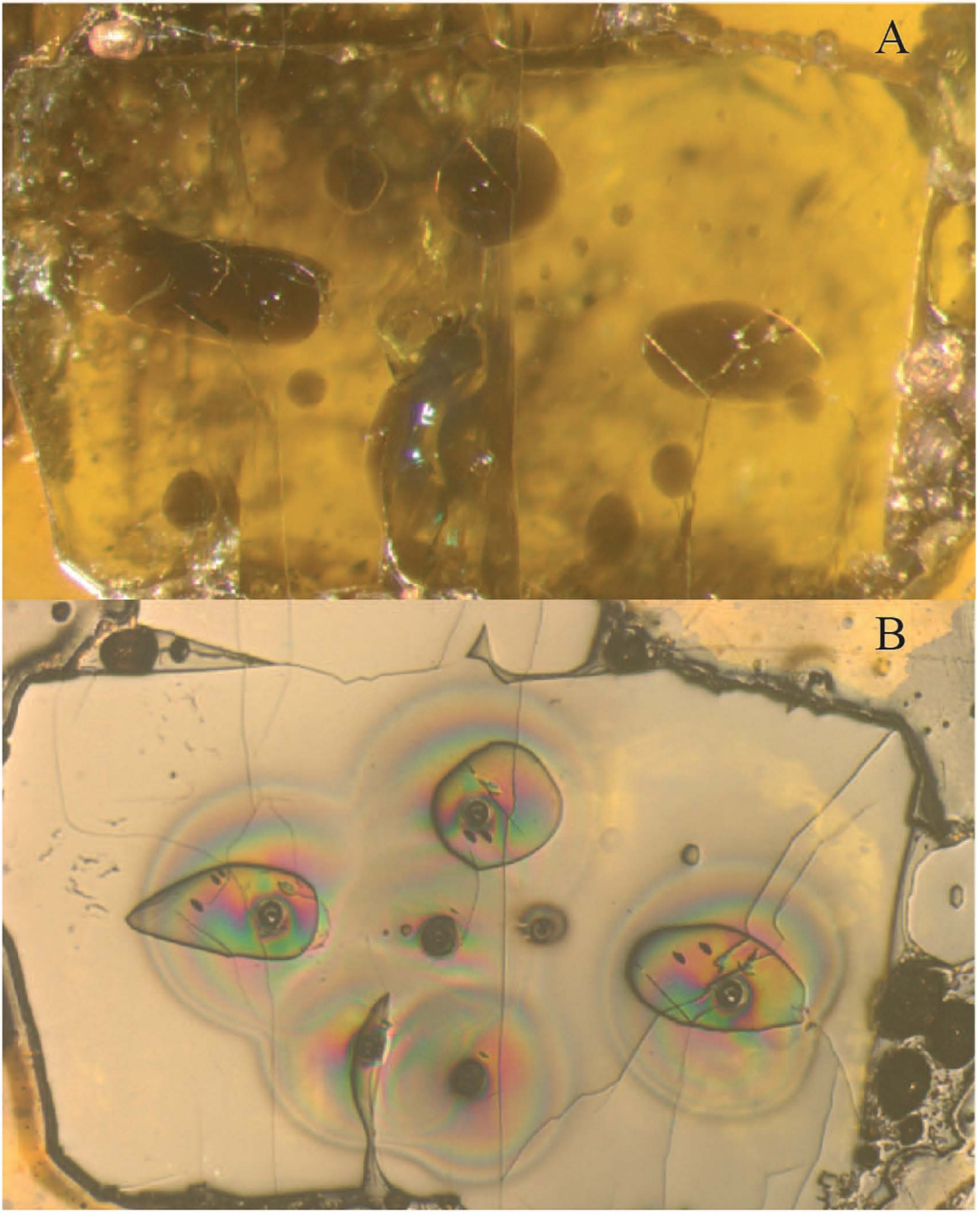

Figure DR2

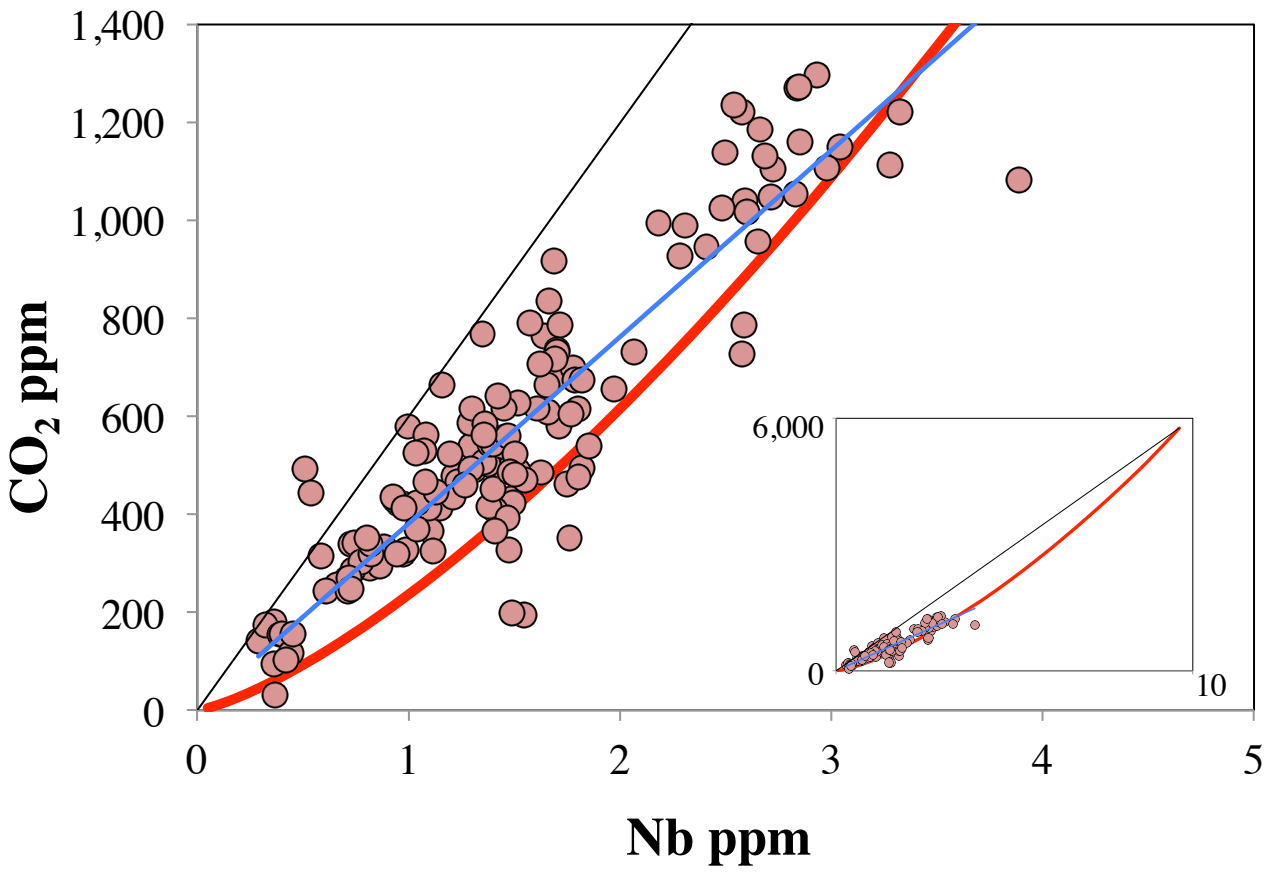

Figure DR3

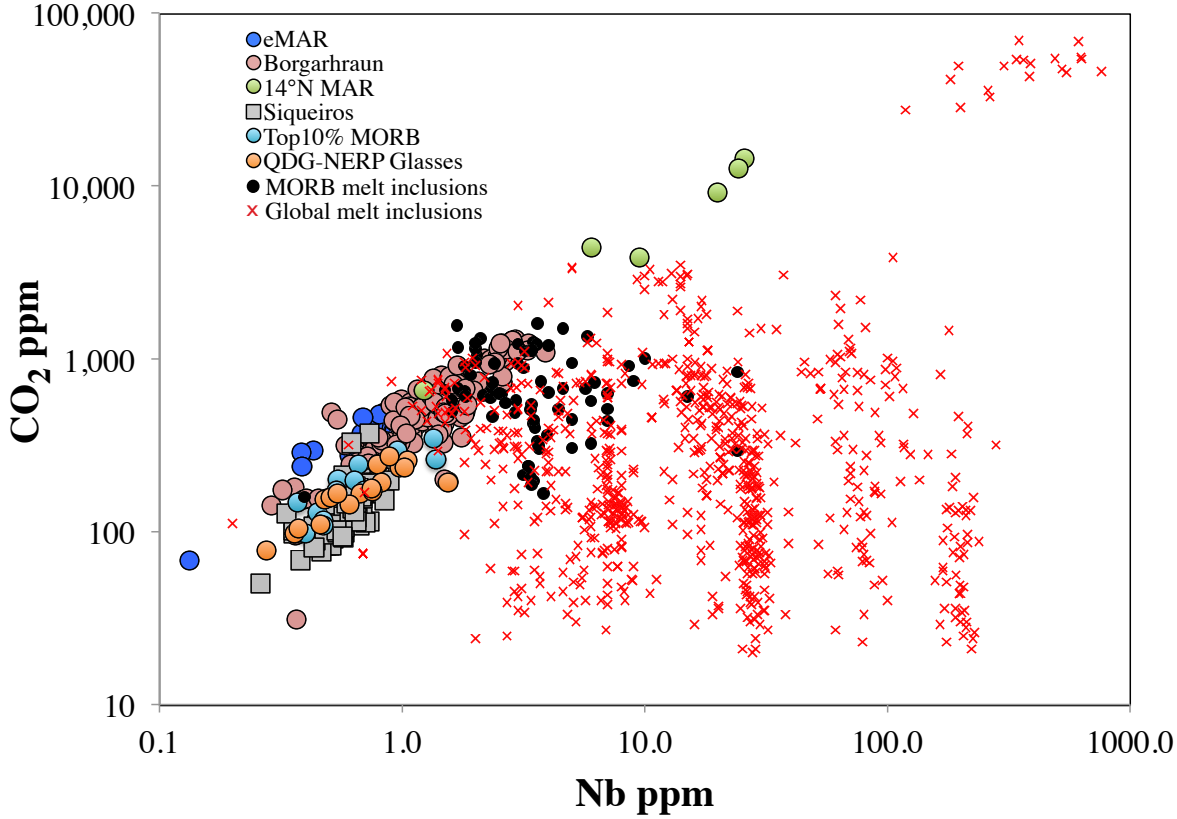
eMAR
Borgarhraun
14°N MAR
Siqueiros
Top10% MORB
QDG-NERP Glasses
MORB melt inclusions
Global melt inclusions
100,000
10,000
1,000
100
10
0.1
1.0
10.0
100.0
1000.0
CO2 ppm
Nb ppm

Figure DR4

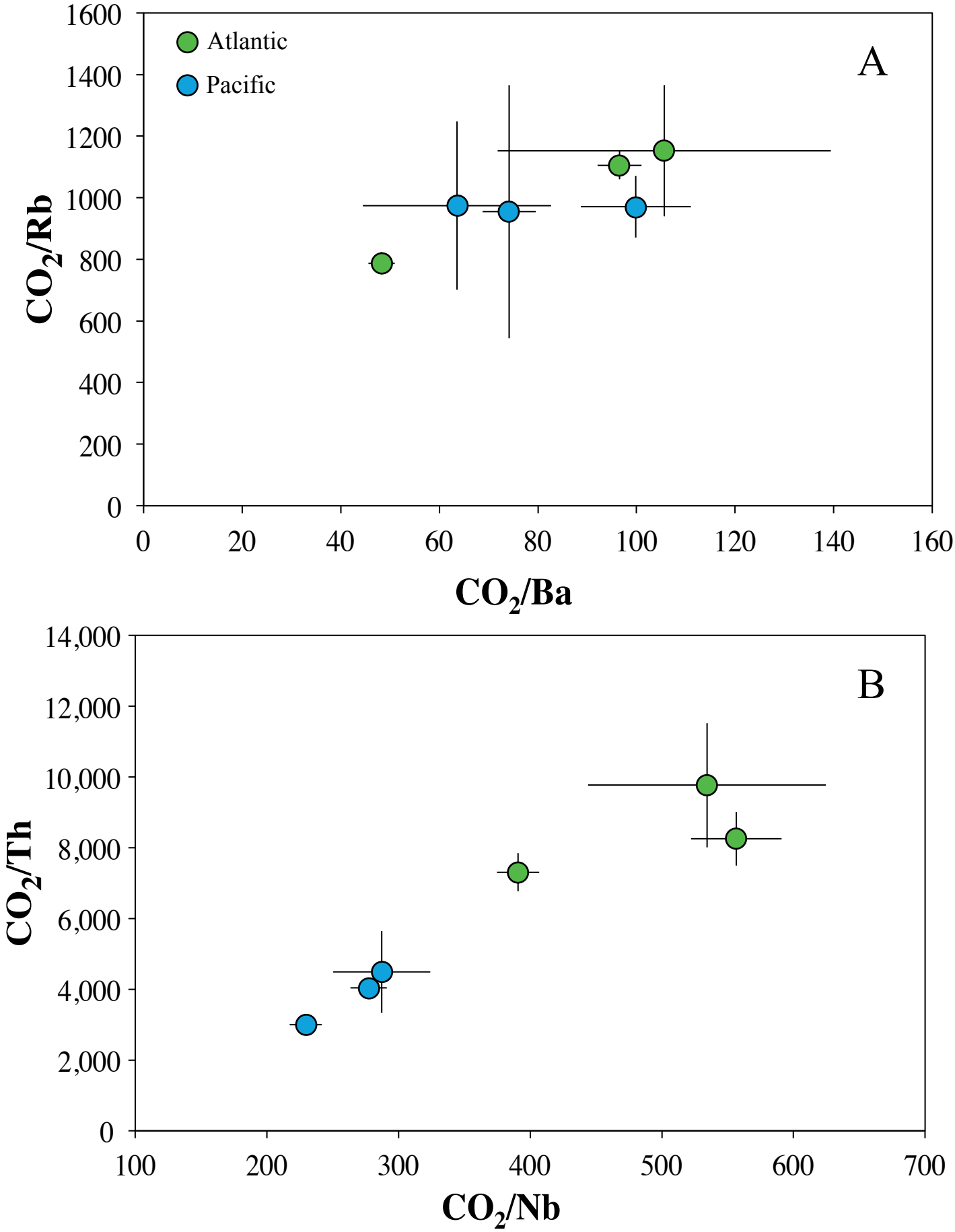
Atlantic
Pacific
A
1600
1400
1200
1000
800
600
400
200
0
CO2/Rb
0
20
40
60
80
100
120
140
160
CO2/Ba
B
14,000
12,000
10,000
8,000
6,000
4,000
2,000
0
CO2/Th
100
200
300
400
500
600
700
CO2/Nb

Figure DR5

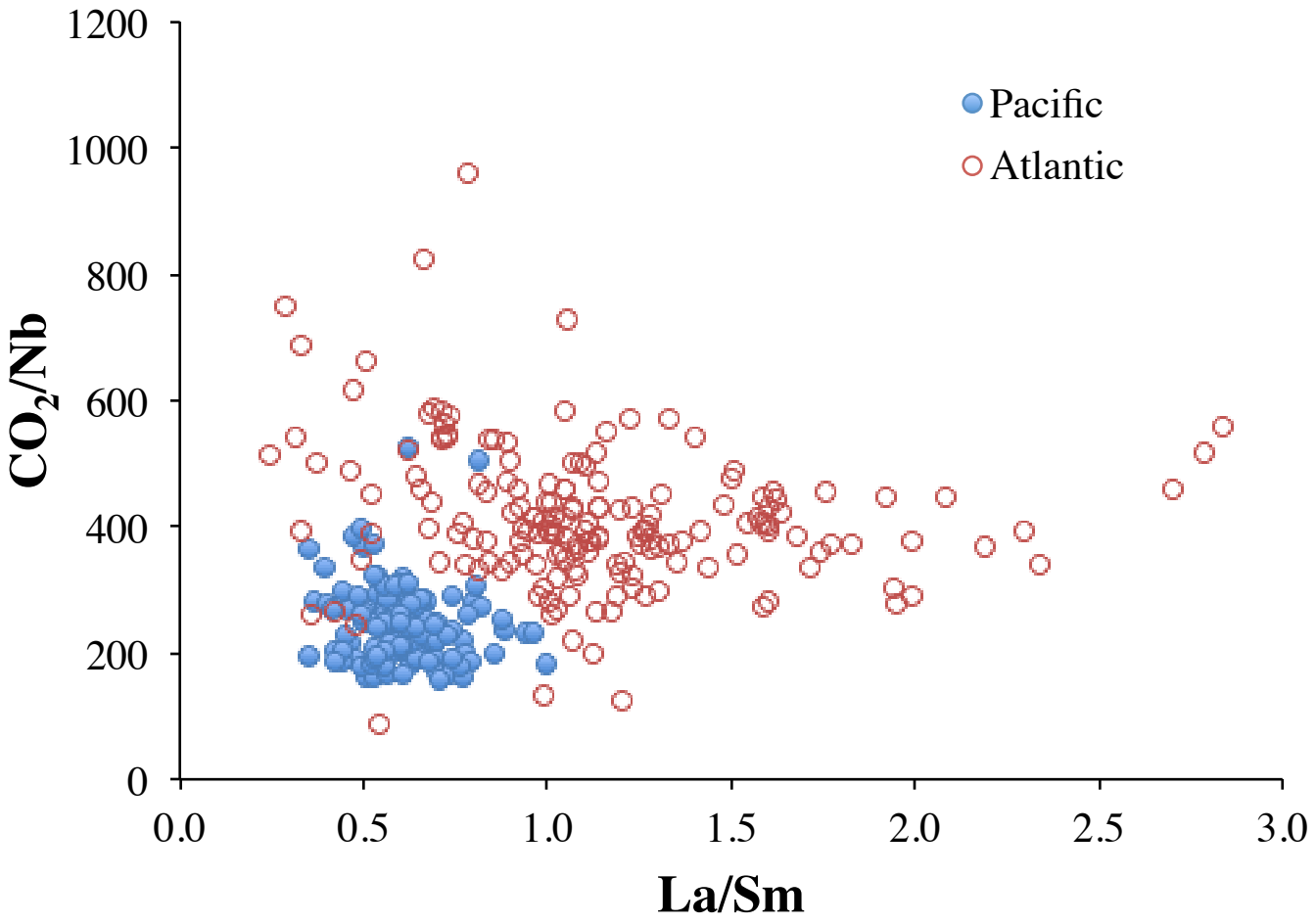
1200
1000
800
600
400
200
0
CO_2/Nb
0.0
0.5
1.0
1.5
2.0
2.5
3.0
La/Sm
Pacific
Atlantic